Soft Matter

PAPER

View Article Online
View Journal | View Issue

Cite this: *Soft Matter*, 2025, **21**, 6963

Deciphering supramolecular and polymer-like behavior in metallogels: real-time insights into temperature-modulated gelation and rapid self-assembly dynamics

Jinnipha Pajoubpong,[af] Marzieh Mirzamani,[a] Diksha Gambhir,[a] Christopher J. Garvey,[b] Xiaobing Zuo,[c] Lilin He,[d] Arnab Dawn *[a] and Harshita Kumari *[ae]

Bis(pyridyl) urea-based gelators, namely **L2** and its isomeric mixture (**L1** + **L2**), are known to self-assemble into 1D architectures capable of inducing supramolecular gelation. Coordination with metal ions such as Ag(I), Cu(II), and Fe(III) introduces structural reinforcement, enabling the formation of distinct 3D networks governed by metal-specific coordination geometries. Here, we present a comprehensive investigation into the temperature-responsive behavior (20–60 °C) of **L2** and **L1** + **L2**, both in the absence and presence of Ag(I), Dy(III), Fe(III), Cu(II), and Ho(III), using real-time small-angle neutron scattering (SANS). To probe long-term structural evolution/kinetics of self-assembly, real-time small-angle X-ray scattering (SAXS) was employed on **L2** + Ag gels, complemented by differential scanning calorimetry (DSC) to evaluate thermal transitions. Our results reveal strikingly divergent gelation behaviors: **L2** forms a highly rigid, covalent polymer-like network, while **L1** + **L2** exhibits remarkable thermal adaptability. Upon metal coordination, the assemblies exhibit pronounced crystallinity and exceptional thermal stability, as evidenced by persistent Bragg reflections and invariant *d*-spacings. Intriguingly, **L2** : Fe (2 : 1) and **L1** : **L2** : Fe (0.5 : 0.5 : 1) in acetonitrile-d_3 (ACN-d_3) deviate from this trend, forming thermally labile amorphous gels. These systems show a complete loss of crystalline order, reduced Porod exponents—indicative of collapsed or branched fiber morphologies—and prominent melting and glass transition events in DSC. Fitting SANS and SAXS data to the correlation length model unveiled insightful nanostructural features. While most systems displayed minimal temperature-induced variation in mesh size or surface morphology, **L2** : Ag in dimethyl sulfoxide-d_6 (DMSO-d_6)/D_2O and **L2** : Fe (1 : 1) in ACN-d_3 exhibited a rare combination of thermally stable correlation lengths and increasing high-*q* exponents—strongly suggesting progressive fiber densification or surface smoothing within a robust gel framework. These findings highlight the tunability and structural resilience of supramolecular gels through precise control of ligand architecture, metal coordination, and temperature, offering valuable design principles for functional soft materials.

Received 24th April 2025,
Accepted 7th August 2025

DOI: 10.1039/d5sm00420a

rsc.li/soft-matter-journal

Introduction

The serendipitous discovery of supramolecular gels has catalyzed extensive research efforts aimed at designing novel gelators for diverse applications while simultaneously elucidating the intricate self-assembly mechanisms governing their unique physicochemical properties.[1–12] A comprehensive understanding of these self-assembly processes necessitates the application of a broad array of advanced characterization techniques. In line with this research trajectory, our previous investigations explored the self-assembly behavior of an isomeric pair of pyridyl-appended bis(urea) gelators.[13] The molecular design of these gelators prioritized the formation of urea tapes *via*

[a] *James L. Winkle College of Pharmacy, University of Cincinnati, 231 Albert Sabin Way, MSB 3109 C, Cincinnati, Ohio 45221, USA. E-mail: kumariha@ucmail.uc.edu, arnabdawn16@gmail.com*
[b] *Technische Universität München, Forschungs-Neutronenquelle Heinz Maier-Leibnitz and Physik Department E13, Lichtenbergstraße 1, 85747 Garching, Germany*
[c] *Argonne National Laboratory, X-ray Science Division, 9700 South Cass Avenue, Lemont, IL 60439, USA*
[d] *Neutron Scattering Division, Oak Ridge National Laboratory, Oak Ridge, TN 37830, USA*
[e] *Materials Science and Engineering, College of Engineering and Applied Science, University of Cincinnati, 2901 Woodside Drive, Cincinnati, Ohio 45221, USA*
[f] *Faculty of Pharmaceutical Sciences, Burapha University, Chonburi 20131, Thailand*

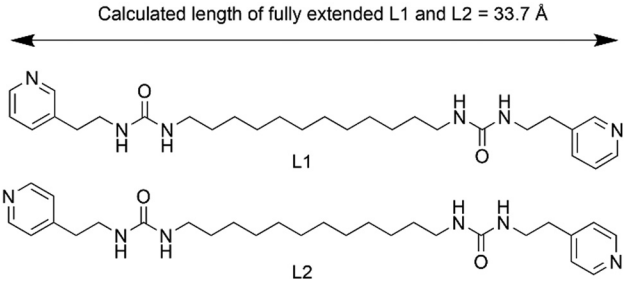

Fig. 1 Chemical structure of **L1** and **L2**.

intermolecular hydrogen bonding, effectively suppressing competing interactions.

Moreover, we examined the impact of metal ion inclusion on gel strength, revealing a significant enhancement exclusively in the presence of Ag(I) for the **L2** gelator (Fig. 1). This effect was attributed to the linear coordination preference of Ag(I), which reinforced the preexisting intermolecular hydrogen bonds among the urea groups. Conversely, in the case of the isomeric mixture of **L1** and **L2**, metal complexation led to gel strengthening irrespective of the type of the metal employed. This distinction arose from the adaptive self-assembly of the **L1** + **L2** mixture, which readily accommodated non-linear metal coordination geometries, thereby stabilizing the network.

Inspired by these intriguing and tunable behaviors, we sought to investigate the influence of external stimuli---specifically temperature—on the metal-ion-mediated self-assembly of these gel systems. Given the sensitivity of supramolecular architectures to thermal variations, subtle changes in temperature can either reinforce or disrupt intermolecular interactions, providing valuable insight into the hierarchy of forces that dictate gel formation.[14–18] Although, the dynamic and reversible nature of interactions characterizes supramolecular systems, in extraordinary circumstances, complementary non-covalent interactions can redefine the balance between flexibility and resilience. This synergy can enhance the strength of the non-covalent interactions to a level where they exhibit behavior resembling covalent bonds. While conventional spectroscopic techniques such as Fourier-transform infrared (FTIR) spectroscopy and nuclear magnetic resonance (NMR) spectroscopy offer molecular-level insights, a deeper understanding of self-assembly processes bridging nanoscopic to macroscopic domains can be achieved through small-angle neutron/X-ray scattering (SANS/SAXS)[19–23] and differential scanning calorimetry (DSC).[24–26] Herein, we present a systematic exploration of the thermal modulation of metal-directed self-assembly in bis(urea)-based supramolecular gels, shedding light on the molecular connectivity and metal/gelator interplay governing their structural evolution and functional adaptability. In addition, we probed the structural evolution in real time to gain insight about hierarchical self-assembly.

Scattering techniques have emerged as invaluable tools for resolving structural hierarchies from the nanometer to micrometer scale. While electron microscopy remains widely employed to visualize gel microstructures, the necessity of a drying step often introduces artifacts that obscure native gel morphologies.[27] In contrast, SANS and SAXS circumvent these limitations by probing the scattering patterns of neutrons and X-rays, respectively, upon interaction with the sample. The non-destructive nature of neutrons enables *in situ* investigations of gels in their native state, eliminating the need for xerogel preparation. By analyzing small-angle scattering profiles, key structural parameters such as nanofiber thickness and length, interfibrillar spacing, and the overall homogeneity of the gel network can be extracted. Consequently, subtle stimuli-responsive changes—imperceptible at the macroscopic level—can be elucidated through variations in fibril density, formation, or disruption. Recent years have witnessed a surge of interest in employing scattering methodologies to probe the self-assembly of supramolecular gels, multicomponent gels, and metallogels.[13,28,29] Additionally, contrast-matching strategies leveraging selective deuteration have proven instrumental in deconvoluting complex self-assembly processes. Previously, our group employed SANS in combination with other characterization techniques to track the slow evolution of a supramolecular gel. This approach also revealed how structural dynamics were significantly altered upon sonication, leading to accelerated gelation.[30] Notably, the time scale for faster gelation process could not be captured due to required long acquisition times. Hence, herein we have employed SAXS, for the first time, to capture fast gelation process.

Complementary to SANS and SAXS, DSC offers critical insights into the thermal behavior of supramolecular gels, capturing gel–sol transitions as well as phase changes such as glass transitions and crystallization—features more commonly associated with covalent polymers. As such, DSC thermograms can help distinguish between supramolecular and covalent molecular connectivity.

Building on our earlier findings where structurally related gelators **L2** and **L1** + **L2** showed distinct metallogelation profiles, this study explores their thermal responses as fingerprints for characterizing the nature and strength of intermolecular interactions. Combined SANS and DSC analyses reveal thermally resilient gel networks exhibiting features typically associated with covalent polymers—an unusual finding for supramolecular systems. Additionally, real-time SAXS was employed to monitor the evolution of gel structure over time, providing critical insight into the kinetics of self-assembly and network formation.

Overall, this gelator system represents a rare example of materials that bridge the dynamic, reversible behavior of supramolecular polymers with the structural rigidity of covalent networks. These findings advance the rational design of hybrid soft materials with tunable mechanical and thermal properties for next-generation applications.

Experimental

Materials

The isomeric bis(pyridyl) urea-based gelators **L1** and **L2** were synthesized following a previously published method.[13] The molecular weight of both **L1** and **L2** is 496.70 g mol^{-1}.

Silver acetate ($Ag(CH_3COO)$), dysprosium(III) chloride hexahydrate ($DyCl_3{\cdot}6H_2O$), iron(III) chloride ($FeCl_3$), copper(II) acetate ($Cu(CH_3COO)_2$), and holmium(III) nitrate pentahydrate ($Ho(NO_3)_3{\cdot}5H_2O$) were purchased from Sigma-Aldrich. Acetonitrile-d_3 (ACN-d_3) was purchased from Acros Organics. Dimethyl sulfoxide-d_6 (DMSO-d_6), deuterium oxide (D_2O), acetonitrile (ACN), and dimethyl sulfoxide (DMSO) were purchased from Sigma-Aldrich.

Gel preparation

20 mg of pyridine-appended bis(urea) ligand **L2**, or a mixture of isomeric pyridine-appended bis(urea) ligands **L1** and **L2** (10 mg each), was transferred into a vial followed by the addition of the metal salt in ratio of either 1 : 1 or 2 : 1 (ligand : metal) (see Tables S1 and S2). Subsequently, 1 mL of solvent(s) was added to achieve a final gelator concentration of 2% w/v. The samples were subjected to sonication for 1–2 min and then heated using a heat gun until a homogeneous solution was obtained (approximately 2–5 min). Finally, the vials were left undisturbed to allow gel formation.

Small-angle neutron scattering (SANS)

Samples for SANS measurements were prepared using a simple mixing method; the components were added in the following sequence: **L2** or **L1** + **L2** (as applicable), followed by the metal salt, and finally the solvent(s) (Tables S1 and S2). In case of binary solvent system with water, the non-aqueous solvent was added first. The gel concentration was kept constant at 2% (w/v). The samples underwent sonication for 1 minute and were subsequently heated until a homogeneous mixture was achieved. The hot solution was then transferred into the sample holder while maintaining elevated temperatures. The prepared samples were allowed to stand undisturbed for approximately 12 hours prior to measurement. SANS experiments were performed at the Quokka beamline, located at the Australian Centre for Neutron Scattering (ACNS) within the Australian Nuclear Science and Technology Organisation (ANSTO).

Three experimental configurations (low-Q, intermediate-Q, and high-Q) were used to cover a wide Q-range of 0.001 $Å^{-1}$ < Q < 0.4 $Å^{-1}$, where the scattering vector $Q = (4\pi/\lambda)\cdot\sin(\theta/2)$, λ is the beam wavelength, and θ is the scattering angle. The sample-to-detector distance of 2 m, 14 m, and 20 m, with λ = 5 Å ($\Delta\lambda/\lambda$ = 0.10) was used to cover high-, mid-, and low-Q, respectively. Backgrounds (empty cell and blocked beam) were also measured and subtracted from scattering data. Measurement time of each sample for the 3 configurations was 115 min at the temperatures of 20, 40, and 60 °C. Direct beam transmission runs were used to scale the averaged data to an absolute cross section form (units of cm^{-1}). All samples were measured inside titanium demountable cells with a quartz window and 2 mm neutron path. Data reduction and normalization were performed using standard techniques with macros developed at ANSTO for IGOR Pro (WaveMetrics, Portland, OR) based on the macros of Kline.[31] The scattering data were then fitted using macros developed by NIST for IGOR Pro (WaveMetrics, Portland, OR)[31] using a summed correlation length and Gaussian peak model. The correlation length model is expressed as:

$$I(Q) = \frac{A}{Q^n} + \frac{C}{1 + (QL)^m} + B \quad (1)$$

where $I(Q)$ is the scattering intensity, L is the correlation length, n and m are Porod and Lorentzian exponents, respectively, A and C are the Porod and Lorentzian multiplicative factors, respectively, and B is the background. The Gaussian peak model is expressed as:

$$I(Q) = D\exp\left(-\frac{(Q - Q_0)^2}{2\sigma^2}\right) + B \quad (2)$$

where D is the scale factor, σ is the peak width (standard deviation), and Q_0 is the peak center.

Small-angle X-ray scattering (SAXS)

To capture real-time self-assembly, we investigated **L1** : **L2** : Fe (1 : 1 : 1) in acetonitrile (ACN), **L2** in dimethyl sulfoxide (DMSO)/H_2O (1/1), **L2** : Cu (1 : 1) in DMSO/H_2O (2/1), **L2** : Fe (2 : 1) in ACN, and **L2** : Ag (1 : 1) sample in a DMSO/H_2O (1/1) solvent system. Samples were prepared using the same protocol as SANS; however, only **L2** : Ag sample showed structural change as a function of time (SI shows overlay of all). In these cases, the SAXS measurements commenced immediately after the sample was transferred into the sample holder to monitor the evolution of the gel structure over a 1-hour period. Quartz capillary tubes with an outer diameter of 2 mm and a wall thickness of 0.01 mm were used as sample holders. The SAXS experiment was conducted at the 12-ID-B beamline of the Advanced Photon Source, Argonne National Laboratory (Lemont, IL). The incident X-ray beam energy was 13.3 keV, and the SAXS data were collected using a Pilatus 2M detector (Dectris Ltd, Baden, Switzerland) with a sample-to-detector distance of 3.6 m. To align a sample, the horizontal position scan was performed and the center of the sample was determined using the horizontal X-ray transmission profile.

To avoid X-ray radiation damage, the SAXS data were then collected by measuring 10 points vertically down the sample holder along the center point with exposure times of 0.5 s each. The first measurement was collected 3.3 min after the sample was made and loaded into the sample holder, and subsequent measurements were taken every 3.3 min until 1 h had elapsed. The solvent system (*e.g.*, 1 : 1 DMSO/H_2O in case of **L2** : Ag metallogel) was measured in the same manner. Two dimensional (2D) SAXS images were converted to 1D curves *via* azimuthally averaging using the beamline software. The 1D curves for the 10 vertical positions were then averaged together for the solvent and gel systems, respectively. Then the solvent background was subtracted from the gel data using a macro created by the beamline scientists for Igor Pro ver. 6.37.

The data were modeled in SasView[32] using the summed correlation length and Lorentzian peak model. The correlation length model is the same as expressed in eqn (1). The Lorentzian

peak model is expressed as:

$$I(Q) = \frac{A}{\left(1 + \left(\frac{Q - Q_0}{\mathrm{HWHM}}\right)^2\right)} + B \quad (3)$$

where A is the scale factor and HWHM is the peak half-width half-maximum. Fittings were also attempted with the Gaussian peak model instead of the Lorentzian peak model, but the Lorentzian peak model fit the peaks better due to SAXS's much greater resolution.

Differential scanning calorimetry (DSC)

All samples were prepared following the same protocol as for the SANS experiments, except that hydrogenated solvents were used. DSC measurements were conducted using a DSC 2500 (TA Instruments). The thermal transition program consisted of three stages: (i) heating from ambient temperature to 90 °C, (ii) cooling from 90 °C to 10 °C, and (iii) reheating from 10 °C to 90 °C, all at a controlled rate of 10 °C min^{-1}. Samples weighing approximately 4–20 mg (Table S14) were sealed in Tzero hermetic aluminum pans with corresponding lids prior to analysis.

Scanning electron microscope (SEM)

Samples were prepared by casting the gels onto silicon wafers, followed by drying under vacuum. Prior to imaging, the samples were coated with gold and analyzed using a FEI Apreo SEM instrument.

Results and discussion

Scattering studies

The *d*-spacing (SANS). SANS data of gel samples were collected at 20°, 40°, and 60 °C to investigate the effect of temperature on the self-assembly of **L2** and the combination of **L1** and **L2** in the presence of metal ions (see SI). The scattering data of **L2** alone and **L2** with metal ions, and the mixture of **L1** and **L2** with metal ions at 20 °C was overlaid in Fig. 2 and 3. Fitting was first attempted to Guinier–Porod model, followed by power law, and correlation length models. Among the three models, the best fit was achieved by fitting to the correlation length model, as determined by best fittings and the low chi-square (χ^2) values. Subsequently, the correlation length model was combined with the Gaussian peak model to effectively capture a small Bragg peak observed at high Q. The Gaussian peak model was used to extract the peak position related to the d-spacing expressed as $d = 2\pi/Q_0$, where Q_0 denotes the peak position. In low molecular weight gel systems, the d-spacing at high Q can be correlated to the dimension of the gelator or highly organized gelator assembly.[3,13,29] The results obtained from fitting to the correlation length and Gaussian peak model are shown in Tables 1 and 2.

For all gels tested, as the temperature rises, the d-spacing remains unchanged, indicating that the primary self-assembled structure is unaffected by heating up to 60 °C. The d-spacing of 21 Å in gel **L2** (**L2** in DMSO-d_6/D_2O (1/1)) can be attributed to the length of one **L2** molecule in partially extended form (Fig. 1). The **L2** molecules stack into a crystalline, repeating nanostructure; resulting in a Bragg peak as observed in the SANS data (Fig. 2b). These repeating units further aggregate to form laminated fibrils.[13] Similar d-spacing of 21 Å was obtained for **L2** : Ag (1 : 1) in DMSO-d_6/D_2O (1/1), while a slightly smaller d-spacing of 20 Å was observed in **L2** : Fe (2 : 1) in DMSO-d_6/D_2O (2/1), which is in agreement with a previous study.[13] Comparatively, a larger d-spacing ranging from 26 Å to 35 Å was found in the remaining gel samples, suggesting the **L2** molecules extend along a single filament. The differences in d-spacing values can originate from the differences in packing modes based on coordination preferences of metal ions. For example, Ag(I)

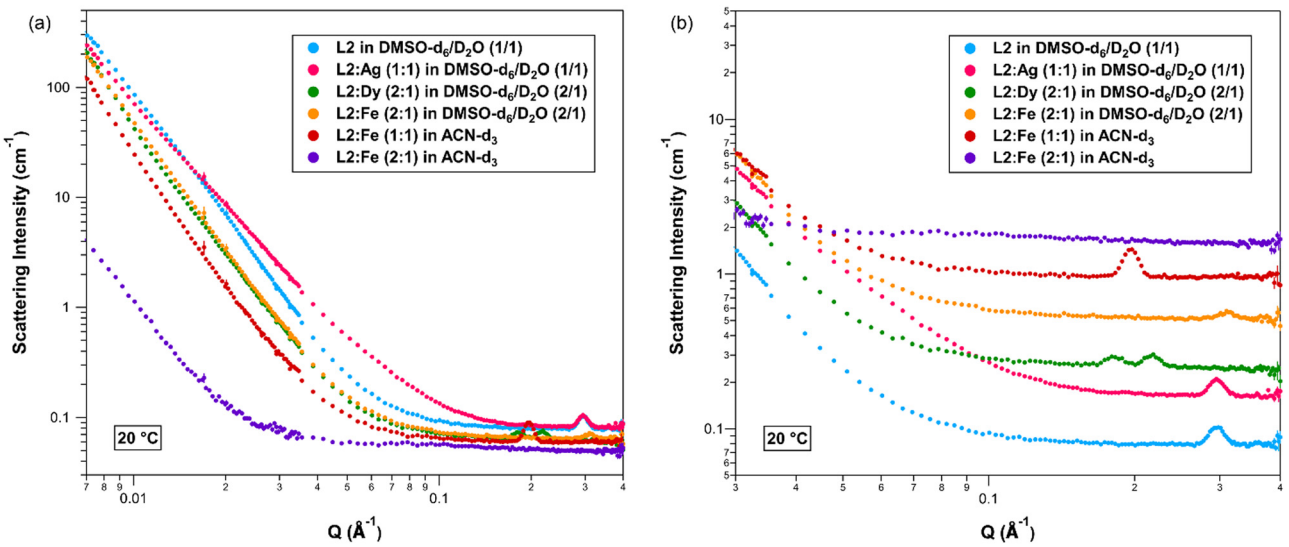

Fig. 2 (a) Overlaid SANS profiles for **L2** gels with and without metal ions at 20 °C; (b) zoomed-in view focusing on the high-Q region ($0.03 < Q < 0.4$). The y-axis values were multiplied by factors of 2^n when n = 1, 2, 3, 4, and 5 for **L2** : Ag (1 : 1) in DMSO-d_6/D_2O (1/1), **L2** : Dy (2 : 1) in DMSO-d_6/D_2O (2/1), **L2** : Fe (2 : 1) in DMSO-d_6/D_2O (2/1), **L2** : Fe (1 : 1) in ACN-d_3, and **L2** : Fe (2 : 1) in ACN-d_3, respectively, to avoid overlapping.

center is likely to coordinate with two pyridyl nitrogen atoms in **L2**, forming a linear 1D coordination geometry[33] (see Fig. S12). Interestingly, two *d*-spacing values of 29 and 35 Å were observed in **L2** : Dy (2 : 1) in DMSO-d_6/D_2O (2/1) as shown in Fig. 2b,

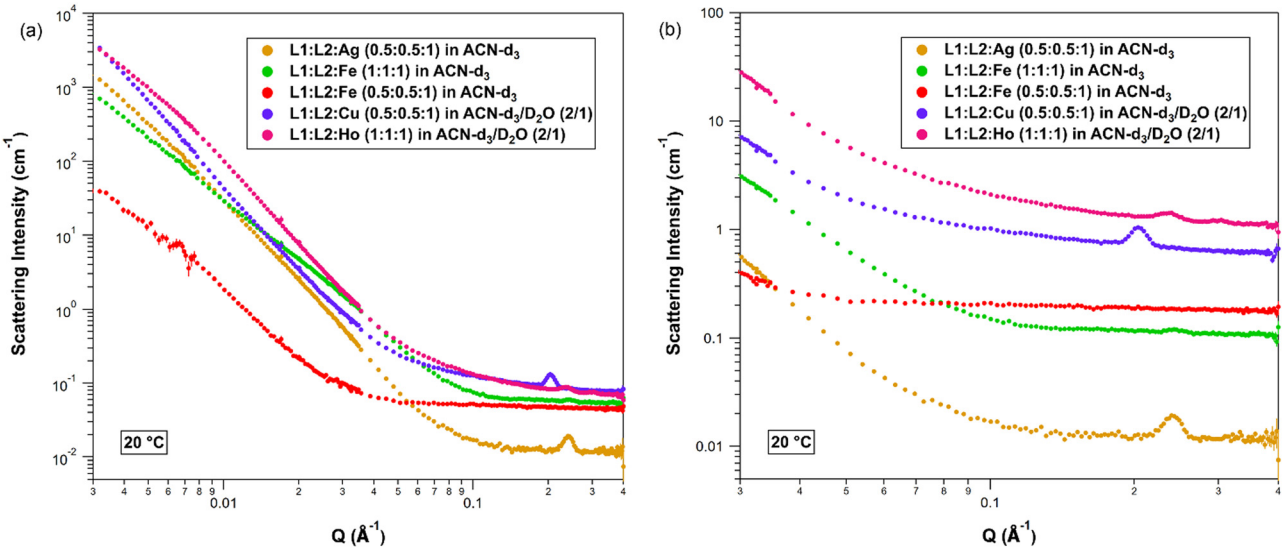

Fig. 3 (a) Overlaid SANS profiles for **L1** : **L2** : metal; (b) zoomed-in ($0.03 < Q < 0.4$) overlaid SANS profiles for **L1** : **L2** : metal. The *y*-axis values were multiplied by factors of 2^n when n = 1, 2, 3, and 4 for **L1** : **L2** : Fe (1 : 1 : 1) in ACN-d_3, **L1** : **L2** : Fe (0.5 : 0.5 : 1) in ACN-d_3, **L1** : **L2** : Cu (0.5 : 0.5 : 1) in ACN-d_3/D_2O (2/1), **L1** : **L2** : Ho (1 : 1 : 1) in ACN-d_3/D_2O (2/1), respectively, for clarity.

Table 1 The correlation length (*L*) and *d*-spacing obtained from fitting the SANS scattering data using the combined correlation length and Gaussian peak model

Ligand : metal (mole ratio) in solvent(s) (volume ratio)	Correlation length (*L*) (Å)			*d*-spacing[b] (Å)		
	20 °C	40 °C	60 °C	20 °C	40 °C	60 °C
L2 in DMSO-d_6/D_2O (1/1)	100.4 ± 0.08	112.7 ± 0.09	234.2 ± 1.4	21.2	21.3	21.2
L2 : Ag (1 : 1) in DMSO-d_6/D_2O (1/1)	77 ± 3	87 ± 4	77 ± 4	21.2	21.3	21.3
L2 : Dy (2 : 1) in DMSO-d_6/D_2O (2/1)	48 ± 4	36 ± 4	22 ± 5	29.0, 34.5	29.1, 34.6	29.1, 34.7
L2 : Fe (2 : 1) in DMSO-d_6/D_2O (2/1)	59 ± 2	40 ± 0.7	61 ± 8	20.2	20.3	—
L2 : Fe (1 : 1) in ACN-d_3	18 ± 4	25 ± 6	22 ± 2	32.0	32.0	32.1
L2 : Fe (2 : 1) in ACN-d_3	5.9 ± 0.4	6.0 ± 0.4	5.5 ± 0.1	—	—	—
L1 : **L2** : Ag (0.5 : 0.5 : 1) in ACN-d_3	65 ± 3	71 ± 1	460.3 ± 7	26.2	26.2	26.0
L1 : **L2** : Fe (1 : 1 : 1) in ACN-d_3	45 ± 0.8	46 ± 0.7	50 ± 0.7	—[a]	26.3	26.2
L1 : **L2** : Cu (0.5 : 0.5 : 1) in ACN-d_3/D_2O (2/1)	63 ± 10	8.6 ± 1.3	5.0 ± 0.1	30.8	30.9	30.9
L1 : **L2** : Ho (1 : 1 : 1) in ACN-d_3/D_2O (2/1)	8.4 ± 0.2	7.8 ± 0.2	7.0 ± 0.2	26.7	26.7	26.9
L1 : **L2** : Fe (0.5 : 0.5 : 1) in ACN-d_3	5.1 ± 0.2	5.1 ± 0.2	5.2 ± 0.2	—	—	—

[a] The Bragg peak was faintly detected. [b] *d*-spacing obtained from SANS fitting corresponds to *d*-spacing 2 from SAXS, which shows two distinct *d*-spacing values.

Table 2 The low-*q* scattering exponent (*n*) and high-*q* scattering exponent (*m*), obtained from fitting the SANS scattering data using the combined correlation length and Gaussian peak model

Ligand : metal (mole ratio) in solvent(s) (volume ratio)	Low-*q* scattering exponent (*n*)			High-*q* scattering exponent (*m*)		
	20 °C	40 °C	60 °C	20 °C	40 °C	60 °C
L2 in DMSO-d_6/D_2O (1/1)	4.0	4.0	4.0	4.0	4.0	4.0
L2 : Ag (1 : 1) in DMSO-d_6/D_2O (1/1)	3.5	3.6	3.8	2.9	2.8	4.0
L2 : Dy (2 : 1) in DMSO-d_6/D_2O (2/1)	4.0	4.0	4.0	3.2	3.2	2.2
L2 : Fe (2 : 1) in DMSO-d_6/D_2O (2/1)	3.9	4.0	4.0	1.4	1.7	1.5
L2 : Fe (1 : 1) in ACN-d_3	4.0	4.0	4.0	2.6	2.6	3.6
L2 : Fe (2 : 1) in ACN-d_3	3.8	3.0	2.1	1.8	2.2	3.0
L1 : **L2** : Ag (0.5 : 0.5 : 1) in ACN-d_3	4.0	4.0	4.0	4.0	4.0	4.0
L1 : **L2** : Fe (1 : 1 : 1) in ACN-d_3	3.2	3.2	3.4	4.0	4.0	4.0
L1 : **L2** : Cu (0.5 : 0.5 : 1) in ACN-d_3/D_2O (2/1)	3.8	3.8	3.9	1.0	1.0	3.1
L1 : **L2** : Ho (1 : 1 : 1) in ACN-d_3/D_2O (2/1)	3.7	4.0	4.0	3.1	2.5	2.3
L1 : **L2** : Fe (0.5 : 0.5 : 1) in ACN-d_3	3.4	3.0	2.4	3.9	4.0	4.0

suggesting two distinct repeating units in laminated fibrils, possibly because of presence of two different coordination geometries driven by Dy(III). Possible coordination modes of Dy(III) are illustrated in Fig. S12; however, it is difficult to determine with certainty which geometries are present in the gel.

While the *d*-spacing values remain constant in most of the gels from 20 °C to 60 °C, this was not the case for **L2** : Fe (2 : 1) in DMSO-d_6/D_2O (2/1) and **L1** : **L2** : Fe (1 : 1 : 1) in ACN-d_3. Rising temperatures can induce the transition from local crystalline ordering to an amorphous structure in **L2** : Fe (2 : 1) in DMSO-d_6/D_2O (2/1), as the peak disappears at 60 °C (Fig. 4a). This means the associated assembly structure is temperature responsive and is related to the coordination preference of Fe(III). Conversely, it can result in a more organized self-assembled filament in **L1** : **L2** : Fe (1 : 1 : 1) in ACN-d_3, as the peak became substantially narrower as the temperature increased from 20 °C to 40 °C (standard deviation decreased from 0.060 to 0.013 $Å^{-1}$), and slightly narrower upon further increase to 60 °C (0.013 $Å^{-1}$ to 0.011 $Å^{-1}$) (Fig. 4b, and Table S10). This contrasting behavior can be correlated with the rigidity and the adaptivity of **L2** only system and **L1** + **L2** system, respectively.[2]

For **L2** : Fe (2 : 1) in ACN-d_3 and **L1** : **L2** : Fe (0.5 : 0.5 : 1) in ACN-d_3, a Bragg peak was not observed in the SANS data at any tested temperatures (Fig. S6 and S11, respectively). This suggests that they do not form crystalline repeating units. Interestingly, these two gels were also the ones that were majorly affected by increasing temperature. The scattering intensity significantly decreased as the temperature increased, indicating that their structures melted and thus could not withstand higher temperatures well.

The low-*q* exponent (*n*), high-*q* exponent (*m*), and correlation length (*L*) (SANS)

The correlation length model provides the correlation length (L) and a high-q exponent (m), often combined with a low-q power law term with exponent (n) to describe scattering from larger structures. In a fibrillar system, the correlation length represents the characteristic length scale over which fibril density fluctuations are correlated, potentially approximating the average spacing within the fibrillar network. In a gel system, the correlation length corresponds to the mesh size of the interpenetrating polymer network.[29] The exponents offer insight into the nature of the scattering inhomogeneities, which can be linked to fibrillar densities across different Q regimes: n arises from the gel network in the low-Q regime (~100s nm length scale) and m reflects local nanostructures in high-Q regime (1–10 nm length scale).[34] The low-q exponent (n), which represents the scattering from the gel network structure, does not change much across the temperature transition as shown in Table 2. A low-q exponent of 3 indicates the scattering from a very rough network, whereas a low-q exponent of 4 indicates scattering from a smooth network. With rising temperatures, a higher value of low-q exponent was found in most of the gel samples with laminated fibrils (*i.e.*, the perfection of the laminates, with the surface being smoother). Conversely, a decrease in low-q exponent was observed with increasing temperatures in **L2** : Fe (2 : 1) in ACN-d_3 and **L1** : **L2** : Fe (0.5 : 0.5 : 1) in ACN-d_3, which have non-laminated fibers, suggesting a reduction in the crosslink density.

The high-q exponent (m), representing scattering from the local nanostructure, was observed to be affected by the temperature in distinct ways. First, as observed in **L2** in DMSO-d_6/D_2O (1/1), the high-q exponent of 4 remains constant as the temperature rises. This suggests that the surfaces of the nanofibrils remain smooth with minimal branching as the temperature increases. However, the increase in correlation length from 100 Å to 230 Å with increasing temperature indicates that the number of entanglements may have decreased, or that

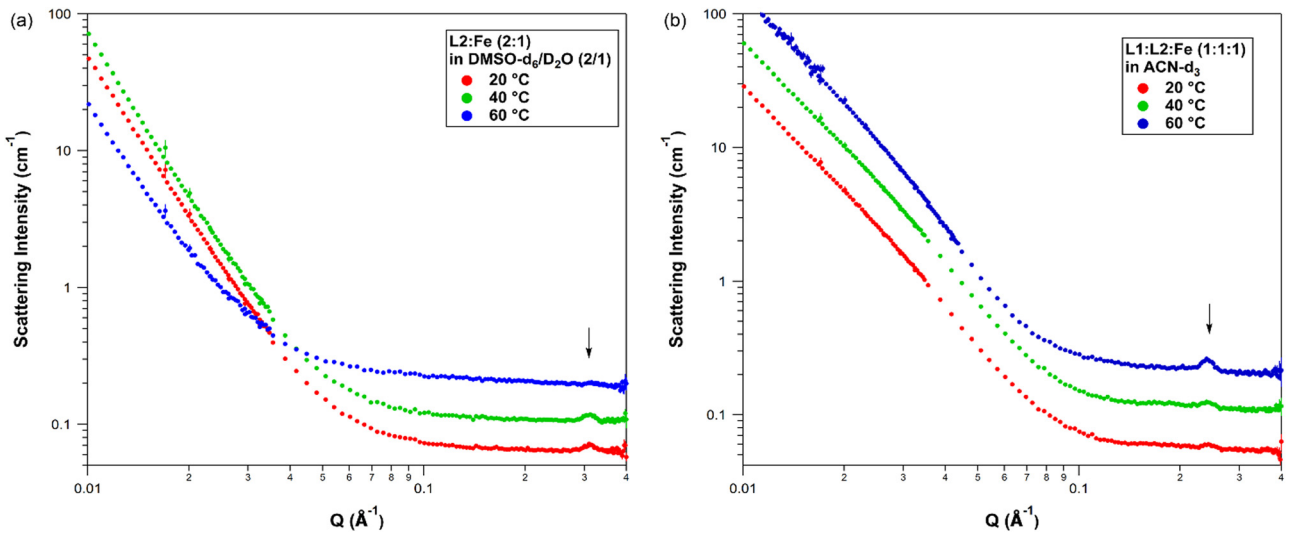

Fig. 4 (a) SANS profiles for **L2** : Fe (2 : 1) in DMSO-d_6/D_2O (2/1) at 20 °C, 40 °C, and 60 °C. The *y*-axis values were multiplied by 2 and 3 for the data at 40 °C and 60 °C, respectively, for clarity; (b) SANS profiles for **L1** : **L2** : Fe (1 : 1 : 1) in ACN-d_3 at 20 °C, 40 °C, and 60 °C. The *y*-axis values were multiplied by 2 and 6 for the data at 40 °C and 60 °C, respectively, for clarity. The arrow indicates the position of the Bragg peak.

the fibers may have lengthened to increase the distance between the existing entanglements.

The addition of a metal seems to reduce the correlation length in most of the gels. However, the correlation length shows no significant change with rising temperatures. In **L2** : Ag (1 : 1) in DMSO-d_6/D_2O (1/1), the correlation length remains between 77 Å and 87 Å across the temperature range. Nevertheless, increasing temperature appears to improve the smoothness of the fibers in this gel, as evidenced by the rise in the high-q exponent from 2.9 to 4.

In the **L2** : Dy (2 : 1) in DMSO-d_6/D_2O (2/1) gel, a reverse trend was observed with rising temperature: a decrease in the high-q exponent from 3.2 to 2.2 alongside a decrease in the correlation length from 48 Å to 22 Å. This suggests that the nanofibrils become more branched, increasing the number of entanglements and thus causing shorter correlation lengths. With a high-q exponent close to 2, the fibers also become close to theta condition, but are still slightly collapsed. This indicates that the fiber–solvent interactions become more favorable as the temperature increases.

Comparing gel **L1** : **L2** : Cu (0.5 : 0.5 : 1) in ACN-d_3/D_2O (2/1) to **L1** : **L2** : Ho (1 : 1 : 1) in ACN-d_3/D_2O (2/1), although both gels show a similar surface scattering as their low-q exponents fall between 3.7 and 4, suggesting surface scattering from somewhat rough to smooth fibers in the gel network. However, their local nanostructure behaves differently with rising temperatures. Both gels form an ordered crystalline nanostructure with a d-spacing of 31 Å in **L1** : **L2** : Cu and of 27 Å in **L1** : **L2** : Ho, indicating the formation of laminated fibrils, as evidenced by the SEM images shown in Fig. S13 and consistent with a previous report.[13] However, due to the very low values of correlation length, it is possible that the gels contain a second phase (non-laminated phase or amorphous region). In this phase, gel **L1** : **L2** : Cu (0.5 : 0.5 : 1) in ACN-d_3/D_2O (2/1) contains rod-like (m = 1.0) fibrils with a correlation length of 63 Å at 20 °C, which become collapsed coils (m = 3.1) with a correlation length of 5 Å as the temperature increases to 60 °C. Meanwhile, the gel **L1** : **L2** : Ho (1 : 1 : 1) in ACN-d_3/D_2O (2/1) starts as collapsed coils (m = 3.1) at 20 °C that then expands to close to theta condition (n = 2.3) at 60 °C. Despite the expansion of the fibers, the correlation length decreases from 8.4 Å to 7 Å as the temperature increases.

The SANS data of **L2** : Fe (2 : 1) in DMSO-d_6/D_2O (2/1) and **L2** : Fe (2 : 1) in ACN-d_3 were compared to understand the effect of solvent on the nanostructure of fibrous network formed. In DMSO-d_6/D_2O, the fibers are swollen at 40 °C ($m \approx 1.67$), but are more akin to branched rods at 20 °C and 60 °C (m = 1.4 and 1.5). The correlation length follows a similar but inverse trend as the temperature increases, with the correlation length staying close to 60 Å but dipping to 40 Å at 40 °C. In ACN-d_3, the gel consists only of an amorphous region. At 20 °C, the high-q exponent (m) of 1.8 and the low-q exponent (n) of 3.8 indicate swollen fibers that appear mostly smooth when observed over long length scales. As temperature rises to 40 °C, these chains are close to theta condition but slightly collapsed (m = 2.2), while the overall gel network is a mass fractal (n = 3) when observed over long ranges. At 60 °C, the fibers collapse into coils (m = 3.0), forming moderately branched networks (n = 2.1).

Moreover, the SANS data of **L2** : Fe and **L1** : **L2** : Fe were compared to understand the effect of Fe concentration on the nanostructure of fibrous network formed. In samples consisting of only **L2**, a higher concentration of Fe in **L2** : Fe (1 : 1) in ACN-d_3 results in a crystalline ordering structure (d-spacing = 32 Å), whereas a lower concentration of Fe in **L2** : Fe (2 : 1) in ACN-d_3 results in almost fully swollen fibers (no Bragg peak, m = 1.8, L = 5.9 Å). However, a reverse trend was observed in samples consisting of both **L1** and **L2**. A higher concentration of Fe in sample **L1** : **L2** : Fe (0.5 : 0.5 : 1) in ACN-d_3 results in smooth fibrils (m = 4, L = 5.1 Å) and no crystalline ordering structure, whereas a lower concentration of Fe in sample **L1** : **L2** : Fe (1 : 1 : 1) in ACN-d_3 results in a crystalline ordering structure. The Bragg peak in sample **L1** : **L2** : Fe (1 : 1 : 1) in ACN-d_3 becomes more pronounced as the temperature increases. Therefore, the formation of a crystalline ordering nanostructure possibly depends on the mole ratio between **L2** and Fe. The **L2**-to-Fe mole ratio among the four gel samples, ranked from lowest to highest, is as follows: 0.25 (**L1** : **L2** : Fe (0.5 : 0.5 : 1) in ACN-d_3), 0.33 (**L1** : **L2** : Fe (1 : 1 : 1) in ACN-d_3), 0.5 (**L2** : Fe (1 : 1) in ACN-d_3), and 0.67 (**L2** : Fe (2 : 1) in ACN-d_3). The crystalline structure begins to form at a ratio of 0.33 at higher temperatures (40 °C and 60 °C) and is found in the sample with a ratio of 0.5 at 20 °C. A concentration of Fe that is too high (**L1** : **L2** : Fe (0.5 : 0.5 : 1) in ACN-d_3) or too low does not result in a crystalline ordering structure.

So far, we have attempted to correlate the d-spacing, correlation length (L), low-q exponent (n), and high-q exponent (m)—extracted from fitting the scattering data—with the structural changes in the gels observed at different temperatures. However, the phenomena associated with the observation such as lamellar stacking, swollen fibers ($m \approx 1.67$), and collapsed fibers, are more complex in nature and mostly relied on the models. To provide complementary evidence supporting the SANS-derived structural interpretations, SEM analysis was performed at 20 °C, as shown in Fig. S13, to confirm the gel morphology at room temperature. In general, fibrous networks are prominent mostly in case of Fe(III) based gel systems. However, it should be noted that due to the different length scales probed by SANS and SEM, microscopy images cannot be directly correlated with the SANS results.

It is important to note that while SANS can reveal hierarchical features of the gel network, it might not distinguish between the various metal–ligand coordination environments or estimate contributions (if any) from coordinated anions. Therefore, the proposed model in Fig. 7 is a simplified illustration to visualize the interplay between multiple types of supramolecular interactions bridging the microscopic and the macroscopic level hierarchies.

Structural development of L2 : Ag (1 : 1) in DMSO/H_2O (1 : 1) over time (SAXS)

SAXS data collection was performed on five systems (see SI); however, only Ag gelator showed changes as a function of time.

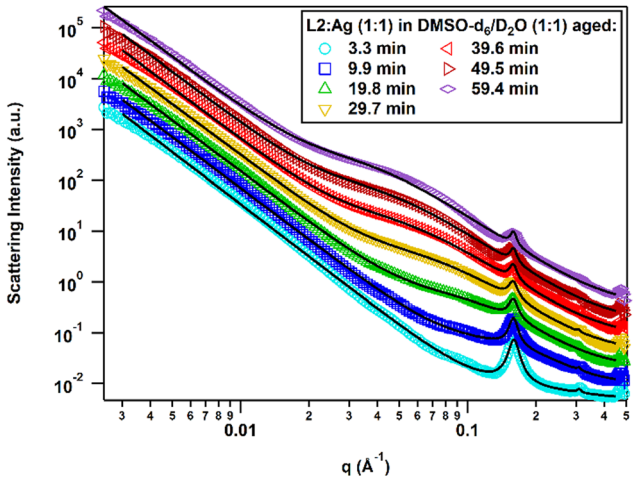

Fig. 5 Overlay of **L2** : Ag (1 : 1) in DMSO/H_2O (1 : 1) SAXS data as a function of time. The curves are offset vertically by powers of 2 for clarity, except for the 3.3 min curve which remains at the original scattering intensity. Solid black lines are the fits to the data using the summed correlation length + 1 (or 2) Lorentzian peak model. Despite manual adjustments to the fit to the 3.3 min data, the broad peak at q = 0.09 Å^{-1} could not be captured well by the model without an extra broad peak model, which was undesirable.

SAXS data for **L2** : Ag (1 : 1) gel in DMSO/H_2O was collected at approximately 22 °C over a period of one hour immediately after the sample was made and loaded into the capillary. The SAXS data overlay is shown in Fig. 5 and important parameters from the data analysis are provided in Table 3. The significant features in the curves include the strong Lorentzian peak at q = 0.15 Å^{-1}, its harmonic peak at q = 0.3 Å^{-1}, and the development of increased mid-q scattering. The presence of a main peak paired with a smaller peak centered at twice the main peak's q-value indicates that the gel forms a layered structure. The peak positions are maintained for the full duration of the experiment, indicating that the primary structure is formed quickly (rapid nucleation) and remains consistent over time. The main peak's position corresponds to a d-spacing of approximately 39.6 Å, which is also twice the length of compact **L2**. This d-spacing and the Porod exponent are close to those obtained with SANS in our previous work.[13]

As the gel structure begins to form, low-q Porod scattering from clusters dominates the scattering from the gel fibers, resulting in a Lorentzian exponent of 4 and extremely small correlation lengths. After 20 min, scattering from the gel fibers becomes strong enough to accurately determine the Lorentzian exponent. As the gel structure develops, the correlation length consistently increases from 3.4 Å to 25.1 Å while the Porod and Lorentzian exponents decrease from 3.4 to 3.3 and 3.2 to 2.9, respectively. The change in the Porod exponent shows that the surfaces of the clusters at longer length scales become slightly rougher while the Lorentzian exponent shows that the gel fibers start as tight coils that slightly loosen over time. Taken together, the gel fibers become slightly less tight coils over time, enabling the distance between the cross-links (*i.e.*, correlation length) to increase as the extent of bundling and branching increases. The combination of the gel fibers becoming less coiled with increasing cross-links causes the clusters to appear rougher at longer length scales.

Differential scanning calorimetry (DSC)

Differential scanning calorimetry is a useful technique to capture thermal events associated with the structural modifications/rearrangements in an assembly triggered by the heat. Therefore, a gel-to-sol phase transition upon heating a gel sample should accompany an endotherm in a heating cycle of a DSC experiment. Similarly, a thermoreversible gel system should also show an exotherm during the cooling cycle of sol. Heating cycles of DSC thermograms associated with various gel systems are presented in Fig. 6. Interestingly, the present gel systems did not follow the above-mentioned conventional patterns. **L2** in DMSO-d_6/D_2O (1/1), **L2** : Ag (1 : 1) in DMSO-d_6/D_2O (1/1), **L2** : Dy (2 : 1) in DMSO-d_6/D_2O (2/1) and **L1** : **L2** : Fe (1 : 1 : 1) in ACN-d_3 did not show any detectable endotherm. Absence of an endotherm in a given heating cycle indicates a practically intact gel structure in the temperature range tested. The presence of strong intermolecular H-bonding, strong metal–ligand coordination, polar interaction *via* pyridine group and involvement of solute–solvent polar interaction are the possible reasons behind the restoration of the gelator scaffold at high temperature. Interestingly, **L2** : Fe (2 : 1) in DMSO-d_6/D_2O (2/1) is the only gel system which showed a gel melting event during the heating cycle. This observation is in agreement with the SANS study which also captured the disappearance of Bragg peak corresponding to the d-spacing at a high temperature signifying crystallinity loss. It is worth noticing that the thermograms of remaining gel samples showed a glass transition temperature (T_g) ranging between 50–70 °C, which is typically associated with the amorphous domain of a covalent

Table 3 Development of **L2** : Ag (1 : 1) in DMSO/H_2O (1 : 1) gel structure as a function of age. The uncertainty in the last significant figure is given in parentheses. The Lorentzian exponent (m) for the 3.3 and 9.9 min data were fixed to 4. d-Spacing 1 corresponds to the larger peak at approximately q = 0.16 Å^{-1}, while d-spacing 2 corresponds to the small peak at q = 0.31 Å^{-1}. The small peak can be seen in each curve, but it could not be consistently fitted

Gel age (min)	Porod exponent (n)	Lorentzian exponent (m)	Correlation length (L) (Å)	d-spacing 1 (Å)	d-spacing 2 (Å)
3.3	3.41(1)	4(0)	3.4(3)	39.31(4)	20.3(2)
9.9	3.35(1)	4(0)	5.10(5)	39.51(4)	20.3(2)
19.8	3.32(1)	3.18(4)	8.4(2)	39.59(4)	—
29.7	3.33(1)	2.96(2)	13.2(2)	39.67(4)	20.3(2)
39.6	3.35(2)	2.92(1)	17.8(2)	39.60(5)	—
49.5	3.36(2)	2.929(8)	21.8(2)	39.50(5)	—
59.4	3.28(2)	2.929(8)	25.1(3)	39.50(5)	—

polymer. The amorphous polymeric nature is also supported by SANS data of **L1** : **L2** : Fe (0.5 : 0.5 : 1) in ACN-d_3, which did not show a Bragg peak at any tested temperatures. In general, appearance of a T_g is more characteristic of gels with mixed ligand systems **L1** + **L2** which were identified as adaptive, and absence of endotherm is more common to the **L2**-based gel systems which were identified as rigid.[2]

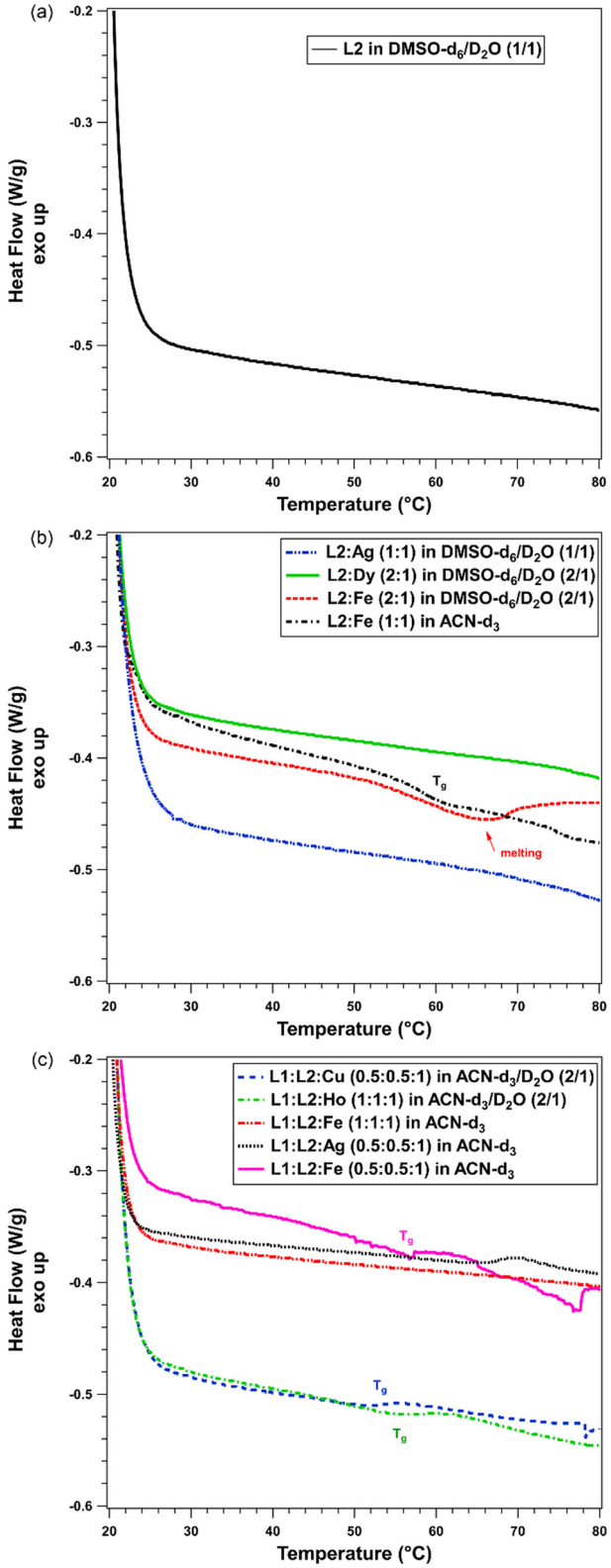

Fig. 6 DSC thermograms of various gel samples with and without metal ions: (a) gel sample without any metal ion, (b) gel samples of **L2** in presence of metal ions, and (c) gel samples of **L1** + **L2** in presence of metal ions.

NMR spectroscopy

^{1}H NMR experiments were performed to address whether the thermal events observed in DSC experiments were associated primarily with the metal–ligand coordination or with the other supramolecular forces involved in gel formation. For simplicity in data interpretation, two gel systems prepared in a single solvent (ACN-d_3): **L1** : **L2** : Fe (0.5 : 0.5 : 1) and **L1** : **L2** : Ag (0.5 : 0.5 : 1) at 1% w/v concentration were selected. In the **L1** : **L2** system, the aromatic proton signals at 7.91 ppm and 8.45 ppm exhibit an upfield and a downfield shift, respectively, with the addition of Fe (Fig. S14a). While the downfield shift clearly indicates a strong metal–ligand coordination, a distinct coordination environment offered by the mixed ligand system and self-assembly driven by the urea groups are collectively responsible for the upfield shift. An increase in temperature further substantiated these shifts with peaks at 333 K appearing at 7.69 ppm and 8.61 ppm, respectively (Fig. S14b). This signifies a coordination-driven rather than an aggregation-driven system at high temperatures. The sharpening of the peaks in response to the temperature was also noticed, owing to the melting of the gel. **L1** : **L2** : Ag system, on the other hand, shows no noticeable peak shifts with increasing temperature, suggesting greater thermal stability or a more rigid network architecture (Fig. S15). This behavior may arise from stronger or less dynamic Ag–ligand coordination, leading to a less thermally responsive supramolecular structure. These findings are consistent with the DSC results as well as the interpretations derived from the SANS results.

Structural elucidation

Temperature dependent studies using SANS and DSC revealed a group of gel systems which were built upon collective contributions from various supramolecular interactions, however, ultimately demonstrated some characteristics of a covalent polymeric system. Bidentate nature of the ligands **L1** and **L2** facilitated the formation of supramolecular polymers, whereas strong metal–ligand coordination amplified the structural rigidity beyond the supramolecular level. The same is also captured in the ^{1}H NMR experiments. Coordination preferences of the various metal ions together with the differentiating adaptivity of **L2** *vs.* **L1** + **L2** ligand systems directed the crystallinity of the above polymeric systems. Rigid gel systems originating from **L2**, which remained essentially unresponsive to the temperature increase, are crystalline in nature. Gels originating from more adaptive mixed-ligand system **L1** + **L2**, on the other hand, are less crystalline in nature and exhibit a T_g characteristic of amorphous domains of a covalent polymer. The combination of supramolecular and covalent characteristics makes the studied gel systems both unique and highly complex.

Moreover, the oxidation state of the metal ion may influence the resulting gel structure. Specifically, lower oxidation state

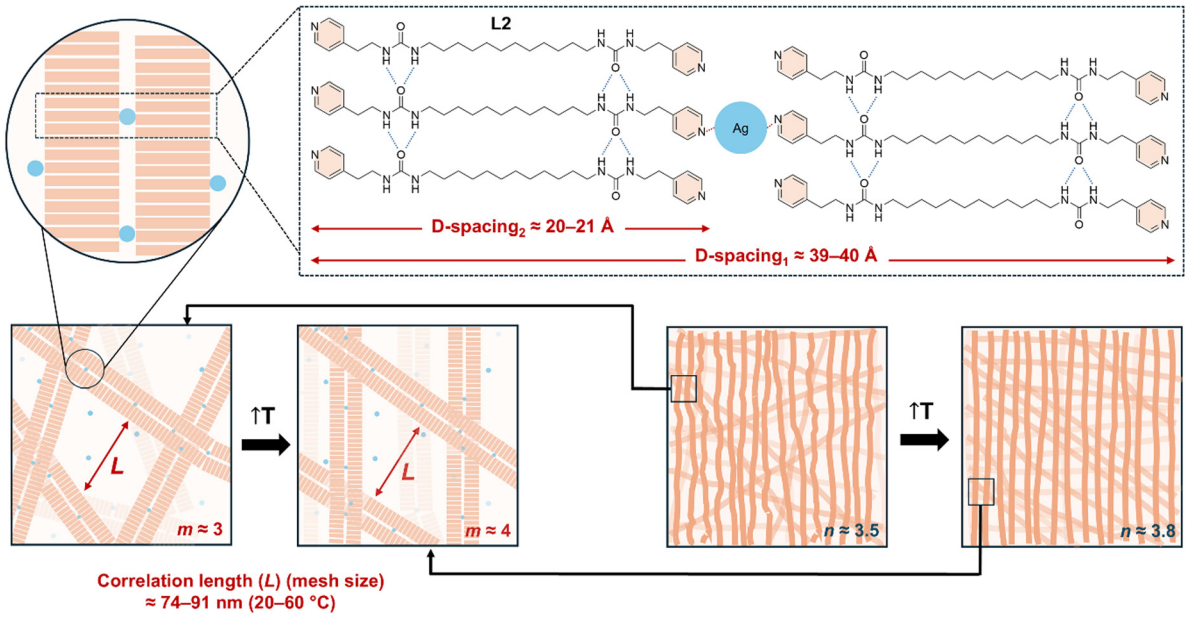

Fig. 7 Simplified illustration of the proposed hierarchical structure of self-assembled gelator **L2** in the presence of Ag(I), where the linear coordination geometry of Ag(I) found to be most reasonable in driving the one-dimensional assemblies. The possible influence of the anions was not taken into the consideration; however, it cannot be ruled out. The minimal structural change observed with increasing temperature suggested that the **L2** : Ag (1 : 1) gel remained thermally stable within the tested temperature range (20–60 °C). The values for each parameter—*d*-spacing, correlation length (*L*), Porod exponent (*n*), and Lorentzian exponent (*m*)—were obtained from SANS and SAXS fitting results.

ions such as Ag^{+} and Cu^{2+} tend to adopt simpler coordination geometries (*e.g.*, linear or square planar), which may result in more uniform, less entangled fibrillar or laminated structures. In contrast, higher oxidation state ions such as Fe^{3+}, Ho^{3+}, and Dy^{3+} often accommodate higher coordination numbers and more diverse geometries, potentially leading to more complex, entangled fibrillar networks or denser architectures.

Time-resolved SAXS study shows rapid self-assembly (<3 min) for Fe and Cu metallogels (SI: not captured effectively with SAXS), while the Ag-complexed system evolves more slowly (reported here), with slightly delayed large-scale structure formation. Initially, low-*q* Porod scattering from aggregates dominates, masking fiber signals and yielding a Lorentzian exponent of 4 with very short correlation lengths. After ~20 min, gel fiber scattering emerges clearly. Over time, the correlation length increases from 3.4 Å to 25.1 Å, while the Porod and Lorentzian exponents decrease from 3.4 to 3.3 and 3.2 to 2.9, respectively. These trends suggest a transition from tightly coiled to more relaxed fibers and increasing cross-linking, which leads to rougher cluster surfaces at larger scales.

It is important to note that although the linear geometry inferred from 1 : 1 metal-to-ligand stoichiometry suggests simple coordination, possibility of more complex assemblies under the influence of anions cannot be ruled out.[35]

Conclusions

In conclusion, the current work captured a unique interplay between supramolecular and nearly covalent intermolecular interactions in a group of gel systems based on a bidentate gel forming ligand and a binary bidentate gel forming ligand mixture, in presence and in absence of various metal ions with wide coordination preferences. The domains with low crystallinity were collectively captured by the temperature responsive Bragg peak using SANS and appearance of T_g in DSC. Similarly, high crystalline domains were captured by the temperature independent Bragg peak in SANS and temperature-independent thermogram in DSC. In addition, we investigated self-assembly/gelation of metallogels in real-time using SAXS.

In the absence of metal ions, the bidentate ligand gels remain robust across the temperature range of 20–60 °C, as indicated by the consistent Bragg peak in the SANS data. The presence of metal ions, however, enables the tuning of the thermally responsive metallogel structure. Depending on the metal ion, the metal coordination geometry influences the arrangement and the correlation of fibers, which is reflected in the correlation length or mesh size. A change in correlation length indicates a change in the structure of the gel, which serves as an indicative parameter for assessing the strength of the metal ion–ligand bonds upon heating. Among the tested metal ions, Ag(I), as a strong linker for self-assembled bidentate ligand, exhibited the strongest bonds within this temperature range, as evidenced by the unchanged correlation length. In contrast, Fe(III) displayed both thermally responsive and thermally independent behaviors, depending on the ligand-to-metal mole ratio and solvent. This is demonstrated by the breaking and reforming of bonds, as indicated by a reduction in the correlation length, which in turn induces structural transformations upon heating. Real-time SAXS data

of **L2**:Ag metallogel showed that the Lorentzian peak was formed within first 3 min, indicating that metal ligation with **L2** occurred almost instantaneously; however, the gel cross-linking and long-range structure developed over time.

While most of the gel systems studied here demonstrated covalent polymer-like behavior, the rigid gels formed with **L2** and relatively adaptive gels formed by **L1** + **L2** showed crystalline and amorphous behavior, respectively. These unique gel systems, initially formed through supramolecular interactions and ultimately demonstrating covalent polymer-like behavior, can be considered a step forward to bridge the gap between supramolecular and covalent assemblies.

Author contributions

HK: conceptualization, formal analysis, project administration, supervision, validation, writing – review and editing, funding acquisition; AD: conceptualization, formal analysis, validation, writing – review and editing; JP: data curation, formal analysis, writing – original draft; MM: data curation, formal analysis, writing – original draft; DG: writing – original draft; CJG: data curation, formal analysis, validation, writing – review and editing; XZ: data curation, formal analysis, validation, writing – review and editing; LH: formal analysis, validation, writing – review and editing.

Conflicts of interest

There are no conflicts to declare.

Data availability

The data supporting this article have been included as part of the SI. The SI contains a table showing the sample compositions, complete fitting results for all SANS data and for the full SAXS time series for the L2:Ag (1:1) in DMSO/H_2O (1:1) gel (plus SAXS data overlays of 4 gels that showed no changes over time), mass of each gel sample for DSC experiments, suggested coordination geometries for metal centers and ligands, SEM images of all gels, and H^1-NMR spectra for selected gels at increasing temperatures. See DOI: **https://doi.org/10.1039/d5sm00420a**

Acknowledgements

The funding for this work was provided by HK research funds (UC start-up and Discretionary funds). This research used resources of the Advanced Photon Source, a U.S. Department of Energy (DOE) Office of Science user facility at Argonne National Laboratory and is based on research supported by the U.S. DOE Office of Science-Basic Energy Sciences, under Contract No. DE-AC02-06CH11357. We also acknowledge the support of the Australian Centre for Neutron Scattering, ANSTO and the Australian Government through the National Collaborative Research Infrastructure Strategy, in supporting the neutron research infrastructure used in this work.

References

1 N. M. Sangeetha and U. Maitra, *Chem. Soc. Rev.*, 2005, **34**, 821–836.
2 S. Banerjee, R. K. Das and U. Maitra, *J. Mater. Chem.*, 2009, **19**, 6649–6687.
3 M.-O. M. Piepenbrock, N. Clarke and J. W. Steed, *Soft Matter*, 2010, **6**, 3541–3547.
4 G. Yu, X. Yan, C. Han and F. Huang, *Chem. Soc. Rev.*, 2013, **42**, 6697–6722.
5 G. Picci, C. Caltagirone, A. Garau, V. Lippolis, J. Milia and J. W. Steed, *Coord. Chem. Rev.*, 2023, **492**, 215225.
6 D. K. Smith, *Soft Matter*, 2024, **20**, 10–70.
7 S. Bianco, S. Panja and D. J. Adams, *Gels*, 2022, **8**, 132.
8 C. R. M. MacDonald and E. R. Draper, *Beilstein J. Org. Chem.*, 2024, **20**, 2608–2634.
9 K. A. Ramya, S. M. M. Reddy, G. Shanmugam and A. P. Deshpande, *Langmuir*, 2020, **36**, 13342–13355.
10 E. R. Draper and D. J. Adams, *Supramolecular Nanotechnology: Advanced Design of Self-Assembled Functional Materials*, 2023, vol. 2, pp. 619–639.
11 C. D. Jones, L. J. Kershaw Cook, A. G. Slater, D. S. Yufit and J. W. Steed, *Chem. Mater.*, 2024, **36**, 2799–2809.
12 J. L. Andrews, E. Pearson, D. S. Yufit, J. W. Steed and K. Edkins, *Cryst. Growth Des.*, 2018, **18**, 7690–7700.
13 A. Dawn, J. Pajoubpong, A. Mesmer, M. Mirzamani, L. He and H. Kumari, *Langmuir*, 2022, **38**, 1705–1715.
14 S. Panja and D. J. Adams, *Chem. Soc. Rev.*, 2021, **50**, 5165–5200.
15 L. Wang, X. Shi and J. Wang, *Soft Matter*, 2018, **14**, 3090–3095.
16 S. Xian and M. J. Webber, *J. Mater. Chem. B*, 2020, **8**, 9197–9211.
17 C. D. Jones and J. W. Steed, *Chem. Soc. Rev.*, 2016, **45**, 6546–6596.
18 S. Debnath, S. Roy, Y. M. Abul-Haija, P. W. J. M. Frederix, S. M. Ramalhete, A. R. Hirst, N. Javid, N. T. Hunt, S. M. Kelly, J. Angulo, Y. Z. Khimyak and R. V. Ulijn, *Chem. -- Eur. J.*, 2019, **25**, 7881–7887.
19 R. Contreras-Montoya, J. P. Smith, S. C. Boothroyd, J. A. Aguilar, M. Mirzamani, M. A. Screen, D. S. Yufit, M. Robertson, L. He, S. Qian, H. Kumari and J. W. Steed, *Chem. Sci.*, 2023, **14**, 11389–11401.
20 A. Dawn, M. Mirzamani, C. D. Jones, D. S. Yufit, S. Qian, J. W. Steed and H. Kumari, *Soft Matter*, 2018, **14**, 9489–9497.
21 H. Kumari, S. R. Kline, S. R. Kennedy, C. Garvey, C. L. Raston, J. L. Atwood and J. W. Steed, *Chem. Commun.*, 2016, **52**, 4513–4516.
22 H. Kumari, S. E. Armitage, S. R. Kline, K. K. Damodaran, S. R. Kennedy, J. L. Atwood and J. W. Steed, *Soft Matter*, 2015, **11**, 8471–8478.
23 K. M. Weigandt, L. Porcar and D. C. Pozzo, *Soft Matter*, 2011, **7**, 9992–10000.

24 H. Wei, H. Yu, A.-Y. Zhang, L.-G. Sun, D. Hou and Z.-G. Feng, *Macromolecules*, 2005, **38**, 8833–8839.
25 D. J. Adams, *J. Am. Chem. Soc.*, 2022, **144**, 11047–11053.
26 M. M. Smith and D. K. Smith, *Soft Matter*, 2011, **7**, 4856–4860.
27 L. L. E. Mears, E. R. Draper, A. M. Castilla, H. Su, Z. Zhuola, B. Dietrich, M. C. Nolan, G. N. Smith, J. Doutch, S. Rogers, R. Akhtar, H. Cui and D. J. Adams, *Biomacromolecules*, 2017, **18**, 3531–3540.
28 L. J. Marshall, M. Wallace, N. Mahmoudi, G. Ciccone, C. Wilson, M. Vassalli and D. J. Adams, *Adv. Mater.*, 2023, **35**, 2211277.
29 D. McDowall, D. J. Adams and A. M. Seddon, *Soft Matter*, 2022, **18**, 1577–1590.
30 M. Mirzamani, A. Dawn, C. J. Garvey, L. He, H. Koerner and H. Kumari, *Phys. Chem. Chem. Phys.*, 2023, **25**, 131–141.
31 S. R. Kline, *J. Appl. Crystallogr.*, 2006, **39**, 895–900.
32 M. Doucet, J. Cho, G. Alina, Z. Attala, J. Bakker, W. Bouwman, P. Butler, K. Campbell, T. Cooper-Benun and C. Durniak, *Zenodo*, 2021, vol. 10.
33 P. Byrne, G. O. Lloyd, L. Applegarth, K. M. Anderson, N. Clarke and J. W. Steed, *New J. Chem.*, 2010, **34**, 2261–2274.
34 R. A. Hule, R. P. Nagarkar, A. Altunbas, H. R. Ramay, M. C. Branco, J. P. Schneider and D. J. Pochan, *Faraday Discuss.*, 2008, **139**, 251–264.
35 J. W. Steed, *Chem. Soc. Rev.*, 2010, **39**, 3686–3699.

